

# Transitional Flow in the Venous Side of Patient-Specific Arteriovenous Fistulae for Hemodialysis

MICHELA BOZZETTO,<sup>1</sup> BOGDAN ENE-IORDACHE,<sup>1</sup> and ANDREA REMUZZI<sup>1,2</sup>

<sup>1</sup>Department of Biomedical Engineering, IRCCS - Istituto di Ricerche Farmacologiche “Mario Negri”, Via G.B. Camozzi, 3, 24020 Ranica, BG, Italy; and <sup>2</sup>Department of Management, Information and Production and Engineering, University of Bergamo, Viale Marconi, 5, Dalmine 24044, BG, Italy

(Received 19 June 2015; accepted 29 November 2015; published online 23 December 2015)

Associate Editor Ender Finol oversaw the review of this article.

**Abstract**—Arteriovenous fistula (AVF) is the first choice for providing vascular access for hemodialysis patients, but maintaining its patency is challenging. AVF failure is primarily due to development of neointimal hyperplasia (NH) and subsequent stenosis. Using idealized models of AVF we previously suggested that reciprocating hemodynamic wall shear is implicated in vessel stenosis. The aim of the present study was to investigate local hemodynamics in patient-specific *side-to-end* AVF. We reconstructed realistic geometrical models of four AVFs from magnetic resonance images acquired in a previous clinical study. High-resolution computational fluid dynamics simulations using patient-specific blood rheology and flow boundary conditions were performed. We then characterized the flow field and categorized disturbed flow areas by means of established hemodynamic wall parameters. In all AVF, either in upper or lower arm location, we consistently observed transitional laminar to turbulent-like flow developing in the juxta-anastomotic vein and damping towards the venous outflow, but not in the proximal artery. High-frequency fluctuations of the velocity vectors in these areas result in eddies that induce similar oscillations of wall shear stress vector. This condition may importantly impair the physiological response of endothelial cells to blood flow and be responsible for NH formation in newly created AVF.

**Keywords**—Hemodialysis, Vascular access, Computational fluid dynamics, Transitional flow, Wall shear stress, Disturbed flow.

---

Address correspondence to Andrea Remuzzi, Department of Biomedical Engineering, IRCCS - Istituto di Ricerche Farmacologiche “Mario Negri”, Via G.B. Camozzi, 3, 24020 Ranica, BG, Italy. Electronic mail: andrea.remuzzi@marionegri.it

Michela Bozzetto and Bogdan Ene-Iordache contributed equally to this work.

## INTRODUCTION

End stage renal disease (ESRD) is a growing global health problem, strictly connected with progressive ageing population and longer survival of patients living on renal replacement therapy (RRT).<sup>24</sup> The majority of these patients are on hemodialysis (HD) treatment, even those awaiting kidney transplantation. A successful HD procedure requires a functional vascular access (VA) to provide safe and long-lasting way to connect patient’s circulation to the artificial kidney. The autogenous arteriovenous fistula (AVF), a surgically created anastomosis between an artery and a vein in the arm, is the VA of choice, as compared to arteriovenous graft (AVG) and central venous catheter (CVC).<sup>41</sup> Despite recent clinical and technological advancements, low primary and secondary patency rates make the AVF the weak part of the HD treatment.<sup>1,8</sup> The most common cause of AVF failure is vascular thrombosis caused by stenosis, which in its turn is caused by severe neointimal hyperplasia (NH).<sup>27,48</sup> Considerable research support the role of local hemodynamic forces as triggering factors for the formation of localized NH, the growth of a layer of resident and infiltrating smooth muscle cells (SMC) that produce abundant extracellular matrix.<sup>36</sup> In this context, it was observed that stenoses usually develop in specific locations of the AVF, the juxta-anastomotic vein (JAV)<sup>3</sup> and, in the cephalic arch, the distal part near termination with the axillary vein.<sup>4</sup>

It is well known that physiologic, pulsatile laminar wall shear stress (WSS) acting on endothelial cells (EC) with a predominant direction activates signaling pathways that induce expression of several atheroprotective and antithrombogenic genes.<sup>20</sup> Among these pathways, EC exposed to unidirectional flow maintain

a quiescent state and induce paracrine signals to underlying SMC. There is convincing evidence that disturbed flow, with low and oscillating WSS, induces selective expression of atherogenic and thrombogenic genes.<sup>10,17</sup> There is less convincing evidence of the WSS pattern that may be related to formation of NH in VA. We have previously suggested, using computational fluid dynamics (CFD) in idealized models of AVF, that in the locations that preferentially develops NH, the WSS is oscillating and in average low in magnitude.<sup>15</sup> Following the same research topic, a CFD study within a realistic *side-to-end* AVF<sup>16</sup> revealed laminar flow in the proximal arterial limb and development of transitional flow leading to multidirectional and reciprocating disturbed flow in the venous segment. This condition may actually induce EC dysfunction. However, the complex blood flow field previously studied in one single case may vary from patient to patient.

The aim of the present study was thus to characterize the blood flow in several real geometry cases, with focus on the near-wall disturbed flow exerted by the transitional flow that occurs in such patient-specific AVF models. We used image-based CFD in four complex AVF geometries with *side-to-end* anastomosis configuration, two placed in the upper arm, namely brachial-cephalic (BC), and two in the lower arm, namely radial-cephalic (RC) fistulae.

## MATERIALS AND METHODS

### *Patient-Specific Data*

The subjects were two males and two females, who participated in a prospective clinical study.<sup>8</sup> As per study protocol,<sup>5</sup> the patients had ultrasound (US) and contrast-enhanced magnetic resonance angiography (CE-MRA) investigations of the non-dominant arm vessels, pre-operatively and 6 weeks post-operatively. US examinations were used to derive patient-specific flow rate waveforms, with the same procedure used previously<sup>14</sup> (see Fig. 1). The CE-MRA image acquisition protocol was described in a previous study by Bode *et al.*<sup>6</sup> to evaluate the feasibility of non-contrast-enhanced MRA for the assessment of upper extremity vasculature prior to VA as compared with CE-MRA. Briefly, the MRA images of the arm used for three-dimensional (3D) reconstruction of the AVF were acquired with a voxel size of  $1.00 \times 1.81 \times 2.50$  mm for BC AVF and  $0.75 \times 1.38 \times 1.68$  mm for RC AVF using a 1.5 T scanner (Intera, 11.3.1, Philips Medical Systems, Best, The Netherlands). Also, at 6 weeks post-operatively, the patients had blood analysis from which we selected hematocrit and total plasma protein

concentration values for viscosity calculation.<sup>47</sup> Demographic and clinical data of the four patients are summarized in Table 1.

### *Three-Dimensional Models of the AVF*

Surface models of the AVF were generated using the Vascular Modelling Toolkit (VMTK).<sup>2</sup> Briefly, the AVF lumen with its limbs, namely the proximal artery (PA), the distal artery (DA), and the venous side comprised of the juxta-anastomotic vein (JAV) and the distal outflow vein (V) were digitally segmented. A polygonal surface was generated by using a gradient-based level set<sup>49</sup> followed by a marching cubes approach.<sup>30</sup> Straight cylindrical flow extensions with a length equal to ten times the mean radius of the lumen profile were then added at the PA, DA, and V of every model to ensure fully development of the flow inside the computational domain (see Fig. 1). Starting from the surface geometry, the internal volume was discretized with the *foamyHexMesh* mesher, which is part of *OpenFOAM* 2.3.1 suite.<sup>43</sup> This mesher produced high quality polyhedral grids, with dominant-hexahedral core cells, that have low orthogonality and are well aligned to the vessel surface. Two thin boundary layers of cells were generated near the wall in all AVF models in order to capture the sharp gradients of velocity in these regions.

In the absence of experimental or direct numerical simulation (DNS) data for validation for patient-specific AVF, we performed the estimation of discretization error by the grid convergence index (GCI) method, which is based on Richardson extrapolation.<sup>9</sup> For one AVF case (RC2) we generated three increasingly density meshes, in particular, a coarse grid made of 147,553 cells (147k), a medium one of 298,829 (299k), and a fine one of 602,110 (602k). We performed transient flow CFD simulations in these three meshes and then estimated the relative error and GCI for mean velocity and TAWSS in the PA (sampling P2), immediately after the anastomosis (P5), and in the JAV (P7). The results of grid convergence study are presented in Table 2. The numerical uncertainty in the fine mesh solution for the mean velocity is 3.0, 6.6, and 59.3% for P2, P5, and P7, respectively. Discretization errors in the calculated TAWSS were 2.5, 70.9, and 161.2% for the PA, immediately after the anastomosis, and in the JAV, respectively. Therefore, we choose to generate similar meshes (~600k) for all AVF models. The characteristics of the grids for numerical calculations for the four AVF models are presented in Table 3 and an example of mesh (RC 2 model) is shown in Fig. S1 (see Supplementary Material on-line).

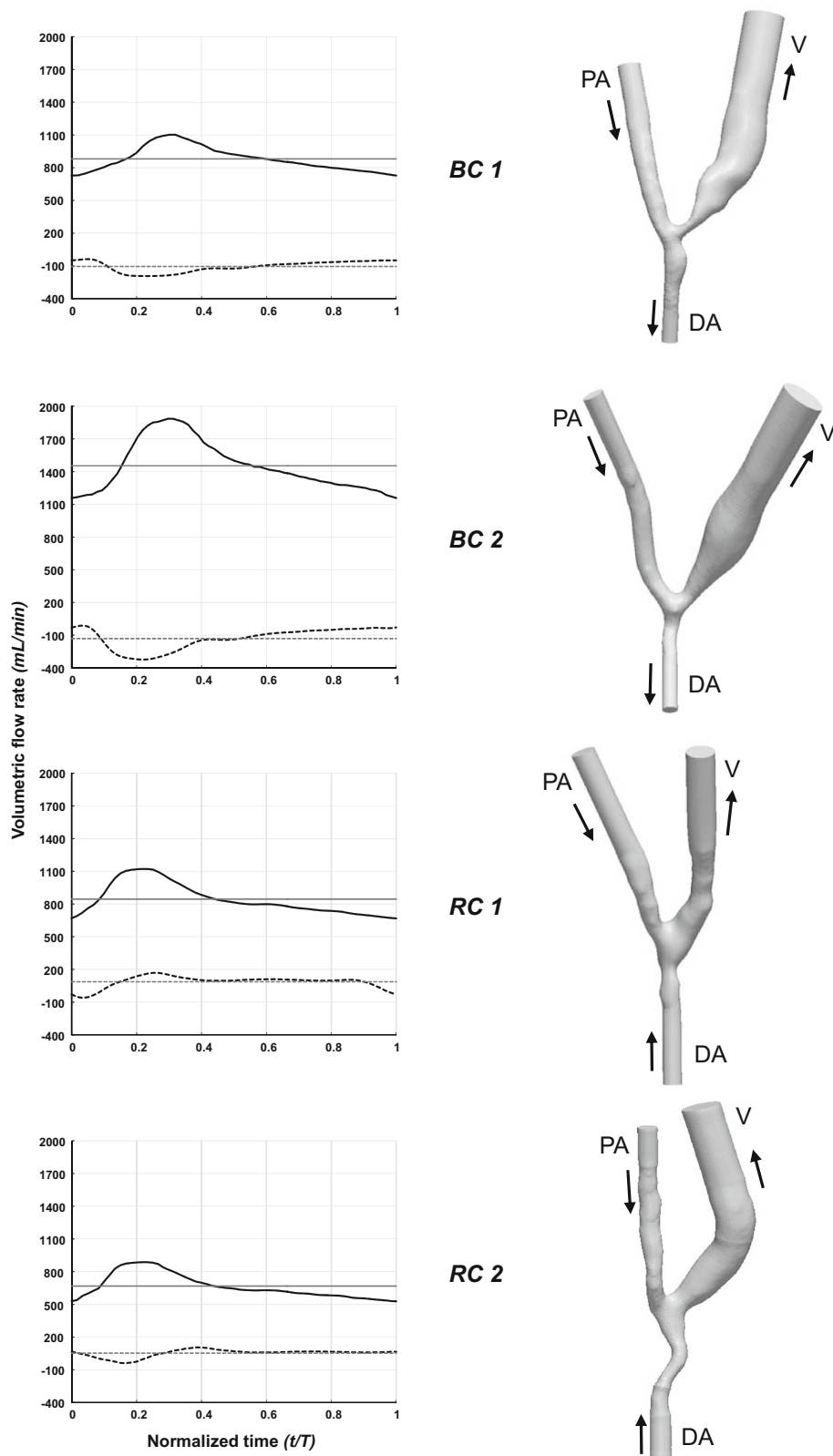


FIGURE 1. Patient-specific blood volumetric flow rate waveforms and 3-D geometrical models of the four *side-to-end* AVF. Continuous and dashed curves represent the blood flow in the PA and DA, respectively. Horizontal lines indicate the time-averaged blood flow rate over the cardiac cycle. Arrows indicate the main direction of blood flow. *BC* brachio-cephalic, *RC* radio-cephalic, *PA* proximal artery, *DA* distal artery, *V* vein

**TABLE 1. Demographic and clinical data of the four patients**

AVF model	BC 1	BC 2	RC 1	RC 2
Gender	Female	Female	Male	Male
Age (years)	44	76	48	77
Arm	Left	Left	Left	Right
Hematocrit (%)	41	36	29	30
Total serum proteins (g/dL)	5.7	6.5	5.4	5.4
Blood viscosity (Poise)	0.031	0.032	0.024	0.036
Hypertension	No	No	Yes	No
Diabetes	No	No	No	Yes

BC brachio-cephalic, RC radio-cephalic.

**TABLE 2. Discretization error of centerline velocity and TAWSS**

	P2		P5		P7	
	$\phi$ = mean velocity	$\phi$ = TAWSS	$\phi$ = mean velocity	$\phi$ = TAWSS	$\phi$ = mean velocity	$\phi$ = TAWSS
$N_1$	602,110	602,110	602,110	602,110	602,110	602,110
$N_2$	298,829	298,829	298,829	298,829	298,829	298,829
$N_3$	147,553	147,553	147,553	147,553	147,553	147,553
$r_{21}$	1.263	1.263	1.263	1.263	1.263	1.263
$r_{32}$	1.265	1.265	1.265	1.265	1.265	1.265
$\phi_1$	153.219	17.168	31.936	9.037	25.779	12.301
$\phi_2$	150.979	18.674	26.132	18.972	46.363	3.142
$\phi_3$	147.371	26.906	27.442	48.179	38.694	17.589
$\rho$	2.04	7.27	6.37	4.62	4.23	1.95
$\phi_{\text{ext}}^{21}$	156.889	16.831	33.629	3.914	13.556	28.167
$e_a^{21}$ (%)	1.5	8.8	18.2	109.9	79.8	74.5
$e_{\text{ext}}^{21}$ (%)	2.3	2.0	5.0	130.8	90.2	56.3
GCI <sub>fine</sub> <sup>21</sup> (%)	3.0	2.5	6.6	70.9	59.3	161.2

The sampling of velocity was performed in three points (P2, P5 and P7) selected along the centerline of the RC2 model AVF in the PA, immediately after the anastomosis and in the JAV as shown in Fig. 4. Corresponding points for TAWSS sampling was done in same cross-sectional plane alongside the PA and the JAV limbs external surface as shown in Fig. 7.

TAWSS Time-averaged wall shear stress, GCI grid convergence index; for the other variables see Ref. 9.

**TABLE 3. Characteristics of the four CFD simulations**

AVF model	BC 1	BC 2	RC 1	RC 2
$N$ mesh cells	605,813	601,671	609,332	602,110
Cell vol ( $\times 10^{-5}$ cm <sup>3</sup> )	(0.014;2.79)	(0.015;2.38)	(0.009;2.21)	(0.010;2.07)
$N$ time steps/cycle	79,727	80,530	29,845	27,737
Delta $t$ ( $\times 10^{-3}$ ms)	13 (5;21)	12 (5;22)	33 (12;48)	32 (15;41)
$Q$ PA (mL/min)	880 (728;1102)	1454 (1159;1886)	844 (669;1121)	668 (529;889)
$Q$ DA (mL/min)	105 (37;192)	131 (12;324)	87 (-60;168)	52 (-39.5;105)
$Q$ PA:DA:V (%)	100:12:88	100:9:91	91:9:100	93:7:100
$Re$ PA	1197 (980;1516)	2385 (1887;3117)	1388 (1080;1879)	1082 (850;1451)
$\alpha$ PA	3.25 (3.23;3.26)	2.79 (2.78;2.80)	3.91 (3.88;3.95)	2.49 (2.48;2.50)

Delta  $t$ , blood flow rates, Reynolds and Womersley numbers are expressed as time-averaged and (minimum; maximum) values over the pulse cycle.  $Q$  PA:DA:V represents the blood flow division ratio between these limbs of the AVF. Cell vol represents the volume of the cells of the mesh expressed as (minimum; maximum).

BC brachio-cephalic, RC radio-cephalic,  $Q$  blood volumetric flow, PA proximal (brachial or radial) artery, DA distal (brachial or radial) artery, V (cephalic) vein,  $Re$  Reynolds number,  $\alpha$  Womersley number.

### CFD Simulations of Blood Flow in the AVF Models

Transient Navier–Stokes equations were solved by using *OpenFoam*, an open-source solver based on the finite volume method.<sup>43</sup> Volumetric flow waveforms

were prescribed as boundary conditions at the inlet of the PA and at the outlet of the DA, while traction-free condition was set at the vein outflow. Vessel walls were assumed to be rigid and blood density was assumed

1.05 g/cm<sup>3</sup>. Blood was modelled as patient-specific, non-Newtonian fluid using the Bird–Carreau rheological model:

$$\mu = \mu_{\infty} + (\mu_0 - \mu_{\infty})[1 + (k\dot{\gamma})^2]^{(n-1)/2}$$

where  $\mu_{\infty}$  is the limiting viscosity at infinite shear rate calculated on the basis of patient's hematocrit and total serum proteins<sup>47</sup> (Table 1),  $\mu_0$  is the limiting viscosity at zero shear rate,  $k$  and  $n$  are constants, and  $\dot{\gamma}$  is the shear rate of the blood.

We used *pimpleFoam*, a transient OpenFOAM solver for incompressible flows, set with second order backward time integration scheme. The convective term in the momentum equation was discretized using a second-order total variation diminishing (TVD) scheme.<sup>55</sup> The linear solvers used were the generalised geometric-algebraic multi-grid (GAMG) for the pressure and the preconditioned bi-conjugate gradient (PBiCG) for the velocity.<sup>43</sup> The pressure and velocity terms were coupled using the pressure-implicit with splitting of operators (PISO) scheme. The *pimpleFoam* solver was set to operate in PISO mode only resulting in very small time steps. This solver adjusts the time step based on a maximum Courant–Friedrichs–Lewy (CFL) number, which we set to 1. Thus, considering the high Reynolds numbers involved, to keep CFL below 1, the numerical solution ran with a high number of time steps per cycle, corresponding to a very high temporal resolution, different for each AVF model (see Table 3). For every simulation, three complete cardiac cycles were solved to avoid start-up transients and only the third cycle was saved for post-processing in 1000 equal time steps. Relevant transient patient-specific CFD parameters are reported in Table 3.

With the aim of studying the influence of blood flow rate decrease on the transitional flow, in one case (RC 2) we performed CFD simulations imposing a half and a quarter of the initial blood flow rate (see Supplementary Material on-line).

### Characterization of the Flow Field

We characterized the AVF flow field phenotype by means of velocity isosurfaces, and categorized the near-wall flow pattern by means of established hemodynamic wall parameters. Blood flow phenotype was also characterized with respect of helicity, a metric applied to quantify the interplay between primary and secondary velocities. As defined by Moffatt and Tsinobor,<sup>37</sup> the helicity of a fluid confined to a domain  $D$  is:

$$H(t) = \int_D (\nabla \times \mathbf{v}) \cdot \mathbf{v} dV = \int_D H_k dV$$

where  $\nabla \times \mathbf{v}$  and  $\mathbf{v}$  are the vorticity and the velocity vectors, respectively, and their inner product is the kinetic helicity density  $H_k$ . A more effective visual inspection of the flow helicity is obtained by normalizing the kinetic helicity density with the velocity and vorticity magnitude, resulting in the localized normalized helicity (LNH)<sup>19,40</sup>

$$LNH = \frac{(\nabla \times \mathbf{v}) \cdot \mathbf{v}}{|\nabla \times \mathbf{v}| \cdot |\mathbf{v}|} = \cos \theta \quad -1 \leq LNH \leq 1$$

where  $\theta$  is the angle between the velocity and the vorticity vectors. By definition, the LNH is a descriptor of changes in the direction of the rotation of flow, the sign of LNH identifying the direction of rotation of the helical structures.<sup>39</sup> Blood flow instability was represented as velocity–time traces normalized by their respective cycle-average velocity for comparison in nine feature points along the centerline. For one case (RC2), we analyzed the power spectral density of resolved velocity at specific probes along the centerline of the AVF.

To quantify reciprocating disturbed flow, we calculated the distribution on the surface of the AVF models of the oscillatory shear index (OSI).<sup>21</sup> Also, aimed at characterizing the multidirectional nature of WSS in disturbed flows, we used the transversal WSS (transWSS) metric proposed by Peiffer *et al.*<sup>44</sup> This metric averages the magnitude of WSS components perpendicular to the mean shear vector on the vessel wall, low values indicating that flow remains approximately parallel to a single direction, while high values indicating changes in near-wall flow direction throughout the cardiac cycle.

Since OSI and transWSS are both time-averaged metrics that cannot describe the frequency of WSS, we generated graphs of WSS vector components in time in one AVF model (RC 2). We calculated its components, namely the  $WSS_{dir}$  in the temporal mean WSS vector direction and  $WSS_{tr}$  in the direction normal to the temporal mean WSS vector.<sup>44</sup>

## RESULTS

The flow complexity can be well appreciated in Fig. 2, where velocity magnitude isosurfaces at mid- and peak-systolic, and mid-diastolic instances are represented. In all AVF models, right after the anastomosis, the bulk flow becomes more adherent to the outer wall of the JAV and the intensity of the secondary vortices increases, therefore velocity isosurfaces lose the well-constructed shape and the smoothness shown in the PA. Figure 3 shows LNH isosurfaces in the four AVF models, corresponding to



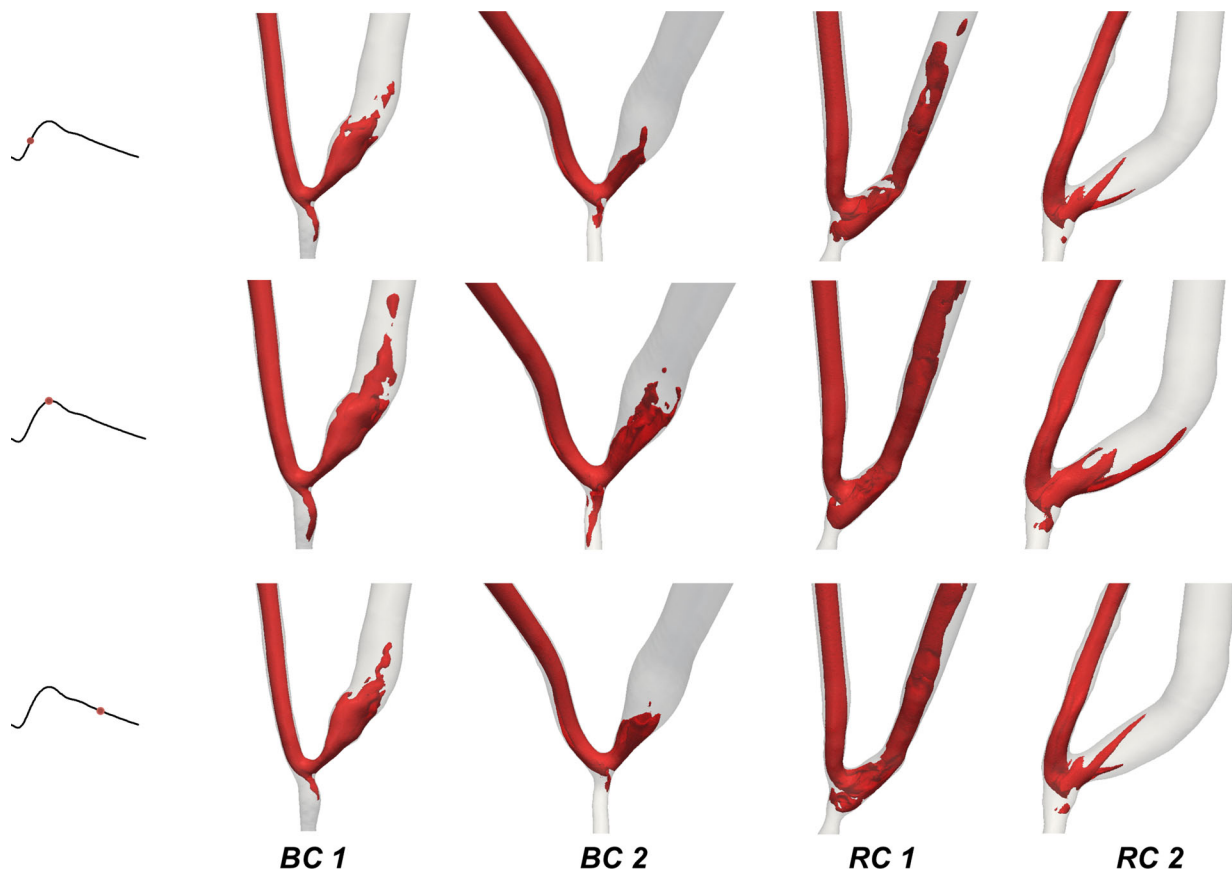


**FIGURE 2.** Velocity magnitude isosurfaces representative for the mid-systolic, peak-systolic and mid-diastolic time-points

mid- and peak-systolic, and mid-diastolic instances. It can be observed that coherent highly helical flow structures originate in the anastomosis towards the vein with both clockwise and counter-clockwise rotation, as classified by the blue and dark red color isosurfaces, respectively. Velocity-time traces of nine feature points sampled consistently along the center-line are shown in Fig. 4. These points were specifically selected across all AVF models: points 1–3 are located in the PA, 4–7 in the JAV, and 8 and 9 more distally in the vein. In every case, velocity traces reveal stable laminar flow in the PA. On the contrary, flow instabilities with frequencies higher than the inflow waveform occur in the JAV (points 4–9), and then start to damp gradually towards the distal part of the vein. This pattern is rather consistent in all four AVF studied, with the exception of points 4 and 5 of BC 1 AVF. Flow is still laminar in these points, due to the existent stenosis, that acts as a nozzle for the flow. Figure 5 shows the power spectral density of the velocity at three featured points selected in the PA, immediately after the anastomosis and in the JAV. In the PA the spectral energy components are present at

frequencies  $< 20$  Hz associated with the cardiac cycle frequencies. On the contrary, in both probes sampled in the JAV, the power spectrum of the velocity signal displays a broad bandwidth with dominant frequencies up to 100 Hz, that decreases linearly at higher frequencies characteristic of turbulent-like flow.

The effects of blood flow rate reduction on transitional flow, calculated only in the RC 2 model, are provided in the Supplementary material on-line (see Figs. S2 and S3), showing that high flow instabilities in JAV are damped by decreasing the flow rate up to a quarter of the original blood flow. The stabilization of velocities in the JAV of RC 2 model with decreasing flow rate is shown in the Supplementary video on-line (MOESM1\_ESM.mp4).

Surface maps of disturbed flow metrics are reported in Fig. 6. For all cases, OSI assumes values lower than 0.1 in the PA, where the near-wall flow mostly maintains the main direction during the entire cardiac cycle. On RC 1 and RC 2, zones of high OSI (0.3–0.5) are located near the anastomosis heel, on the inner wall of the JAV and on the DA. Both BC AVF models have a wider area of high OSI on the JAV. Multidirectional

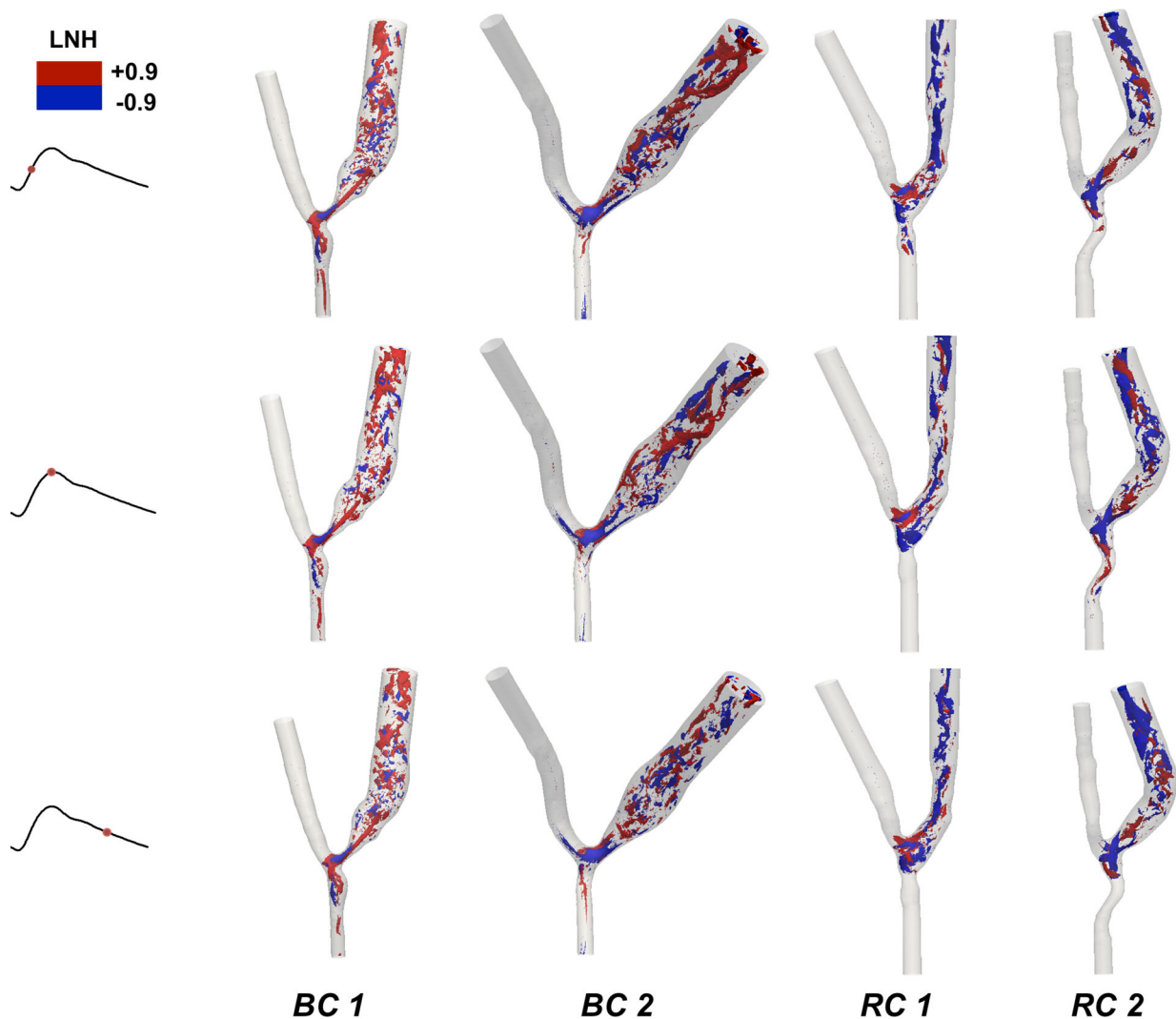


**FIGURE 3.** LNH isosurfaces representative for the mid-systolic, peak-systolic and mid-diastolic time-points. LNH localized normalized helicity. Threshold values of LNH ( $\pm 0.9$ ) are used for the identification of clockwise and counter-clockwise rotation of the helical structures

flow, as characterized by medium-to-high transWSS ( $\text{transWSS}^* > 0.2$ ), is consistently located on the anastomosis floor and the JAV in all models. Such patterns of transWSS indicate that shear vectors change direction throughout the cardiac cycle on the JAV surface, while they remain approximately parallel to the dominant direction of near-wall flow on the PA and DA. Actually, the fast fluctuating transient flow in the JAV induces rapid changes in WSS vectors. This is exemplified in Fig. 7 that shows time traces of the WSS components, at fifteen feature points along the external surface of RC 2 model. Flow instability, starting from point 6, appears evident. High frequency fluctuations, either in  $\text{WSS}_{\text{dir}}$  or in  $\text{WSS}_{\text{tr}}$  and the high values of  $\text{WSS}_{\text{tr}}$  in the JAV, sampled at points 7–12, reveal the multidirectional nature of the near-wall flow. Moving from the PA towards the vein,  $\text{WSS}_{\text{dir}}$  values decrease and  $\text{WSS}_{\text{tr}}$  values increase simultaneously, confirming

the evolution from unidirectional flow in PA to multidirectional flow in the vein. Starting from point 13 the high frequency oscillations start to damp gradually, both for the  $\text{WSS}_{\text{dir}}$  and the  $\text{WSS}_{\text{tr}}$  component.

## DISCUSSION

In the present pilot study, we investigated the nature of the flow in four patient-specific AVF models, by employing high-resolution CFD simulations with realistic blood flow conditions. The numerical simulations allowed a detailed characterization of the flow field in all four AVF models, focused on flow instability and its influence on the near-wall disturbed flow.

Our results showed that when blood leaves the PA and enters the anastomosis, a fast transition from laminar to turbulent-like flow consistently develops and

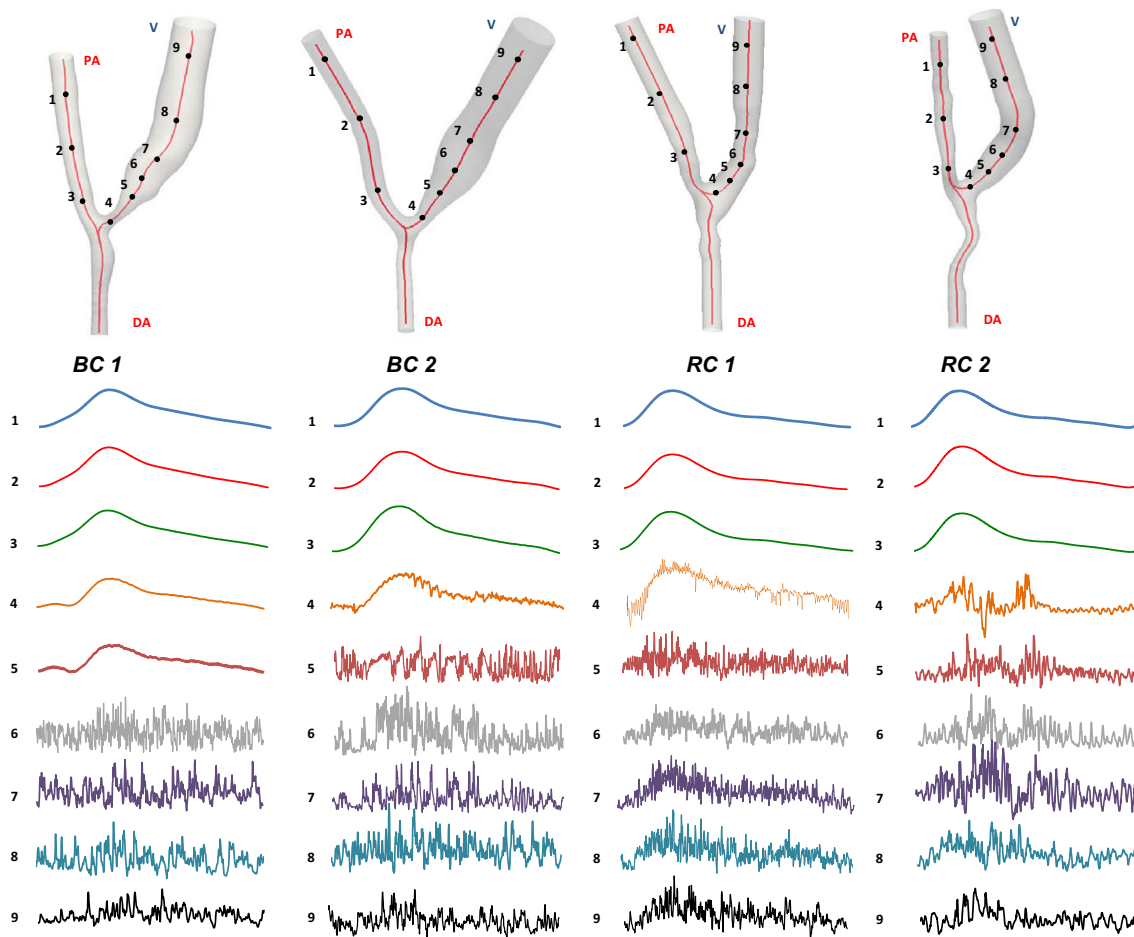


**FIGURE 4.** Velocity-time traces, normalized by their respective cycle averages, at nine selected feature points along the centerline of the four AVF

persists along the venous side of the AVF. Our results are in line with the study of Marie *et al.*<sup>33</sup> who found spiral laminar flow *in vivo*, representative of physiological blood flow in the PA, but chaotic flow, consistent with velocity high fluctuations, in the JAV. Flow entering the anastomosis from the PA has a significant change in direction and impinges on the opposite wall of the anastomosis, creating vortices and secondary flows, in line with those obtained by other authors in patient-specific models of AVF<sup>22,50</sup> and in AVG.<sup>28,31</sup> In well-developed turbulent flows, the spectrum of turbulent energy displays three ranges, the first of large scale eddies which carry most of the energy, the second where large eddies fragment by vortex stretching due to inertial forces, and the third one of smallest scale eddies which are strongly affected by the viscosity.<sup>29</sup> We have found turbulent-like flow patterns of power spectral density of streamwise velocity in the JAV of patient-specific AVF for HD, in line with those found by Browne *et al.*<sup>7</sup> using high-resolution CFD in an idealized geometry of *side-to-end* AVF. It seems clear that flow instabilities repre-

sentative of transitional flow, either in RC or in BC AVF models, are related to high frequency oscillations in the velocity field, present in the JAV and damping towards the distal part of the vein. Such flow instabilities are rarely observed and documented in physiological, as well as in pathological conditions. Other recent high-resolution CFD studies have revealed the presence of laminar flow instabilities and possible transitional flow in intracranial aneurysms.<sup>26</sup> Valen-Sendstad *et al.*<sup>51</sup> found transient flow with energetic velocity fluctuations up to 100 Hz in the carotid siphon of intracranial bifurcation aneurysms, that are by nature vessel segments with sharp bends and large variations in cross sectional area. The pathophysiological role of these flow conditions in aneurysmal disease is still not clear at the moment.

We identified development of reciprocating disturbed flow (high OSI) near the anastomosis floor, on the DA and more on inner wall of the JAV. Multidirectional disturbed flow developed consistently in all models on the anastomosis floor and on the JAV walls



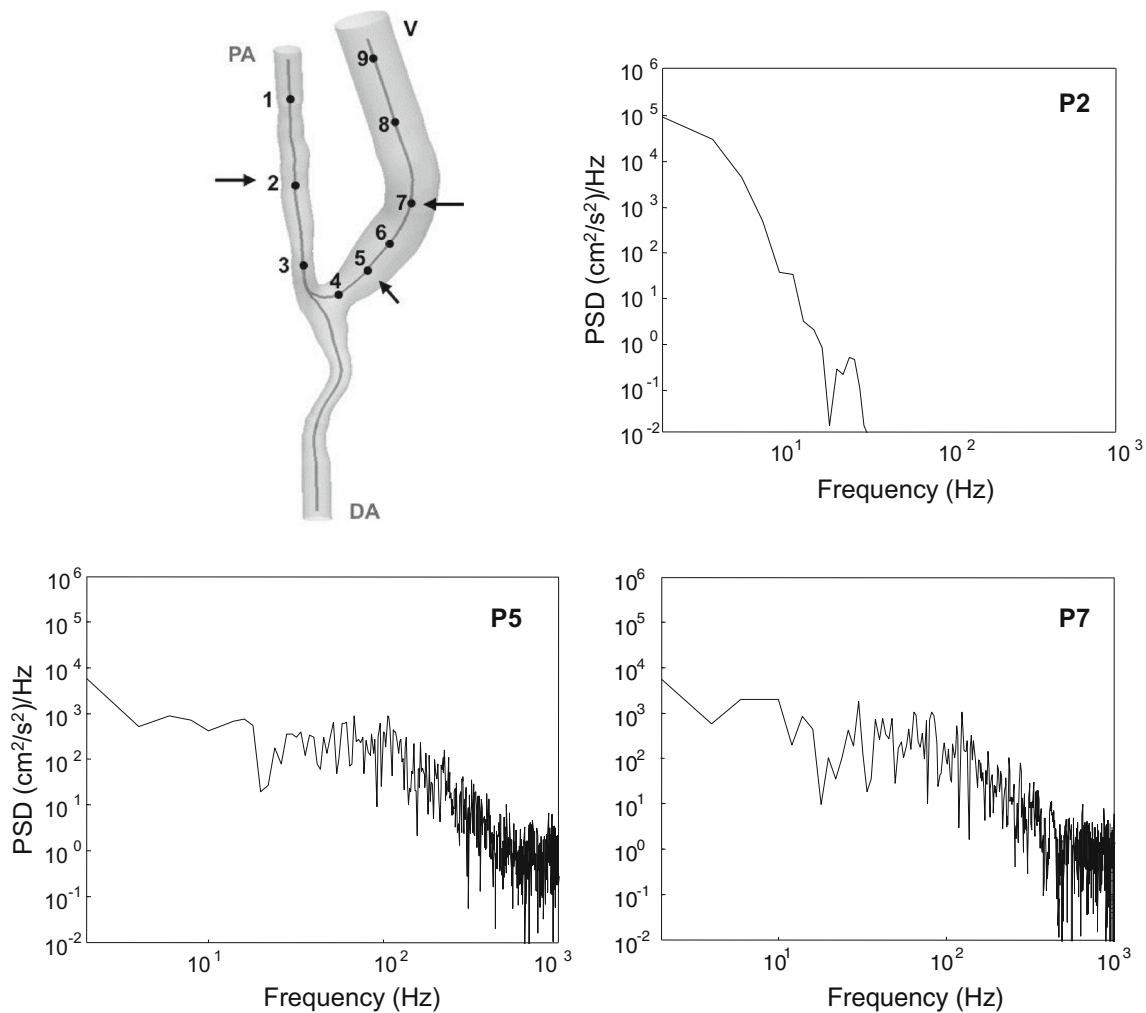


**FIGURE 5.** Power spectral density of velocity sampled at three feature points of RC2 model AVF. The three points were selected specifically along the centerline of the AVF (P2, P5 and P7, indicated by the arrows), respectively, in the PA, immediately after the anastomosis and in the JAV. PA Proximal artery, DA distal artery, V vein, PSD power spectral density

(see Fig. 6b), which corroborated our finding in only one RC AVF model.<sup>16</sup> By representing the WSS vector components traces throughout the cardiac cycle (see Fig. 7), we were able to show that the nature of reciprocating flow developed on the DA and on the JAV walls are different. While the DA experienced pure reciprocating flow at the frequency of the heart rate, the oscillations of the WSS on the JAV were at high frequencies, induced by the fluctuations of the velocity vectors at this level.

As far as we are aware, our study is the first detailed characterization of the transitional flow field in a series of patient-specific AVF models, and focused on disturbed flow as a potential trigger for NH. Flow patterns were conveniently described and visualized using velocity and hemodynamic wall parameters commonly used to characterize disturbed flow. Counter-rotating intertwined fluid structures visualized by LNH consistently charac-

terized the flow in the JAV of the AVF and, to the best of our knowledge, this metric has never been used to characterize the flow field inside the AVF. It was previously proposed that the presence of a centralized, predominating one-vortex secondary flow, stabilizes the flow field in the distal venous segment of helical designed AVG, avoiding the breakdown in multiple vortex patterns and fostering the mitigation of transitional effects downstream of the anastomosis.<sup>52</sup> In light of above-mentioned speculation, the localization and the effects of helical structures could be better defined studying different configurations of anastomosis and different VA. Our investigation of the components of WSS vector also demonstrates that the JAV is characterized by oscillating  $WSS_{dir}$  and  $WSS_{tr}$  also beyond high OSI zones, leading to the need of further investigations to identify hemodynamic wall parameters of disturbed flow areas to predict the risk of stenosis formation in AVF.

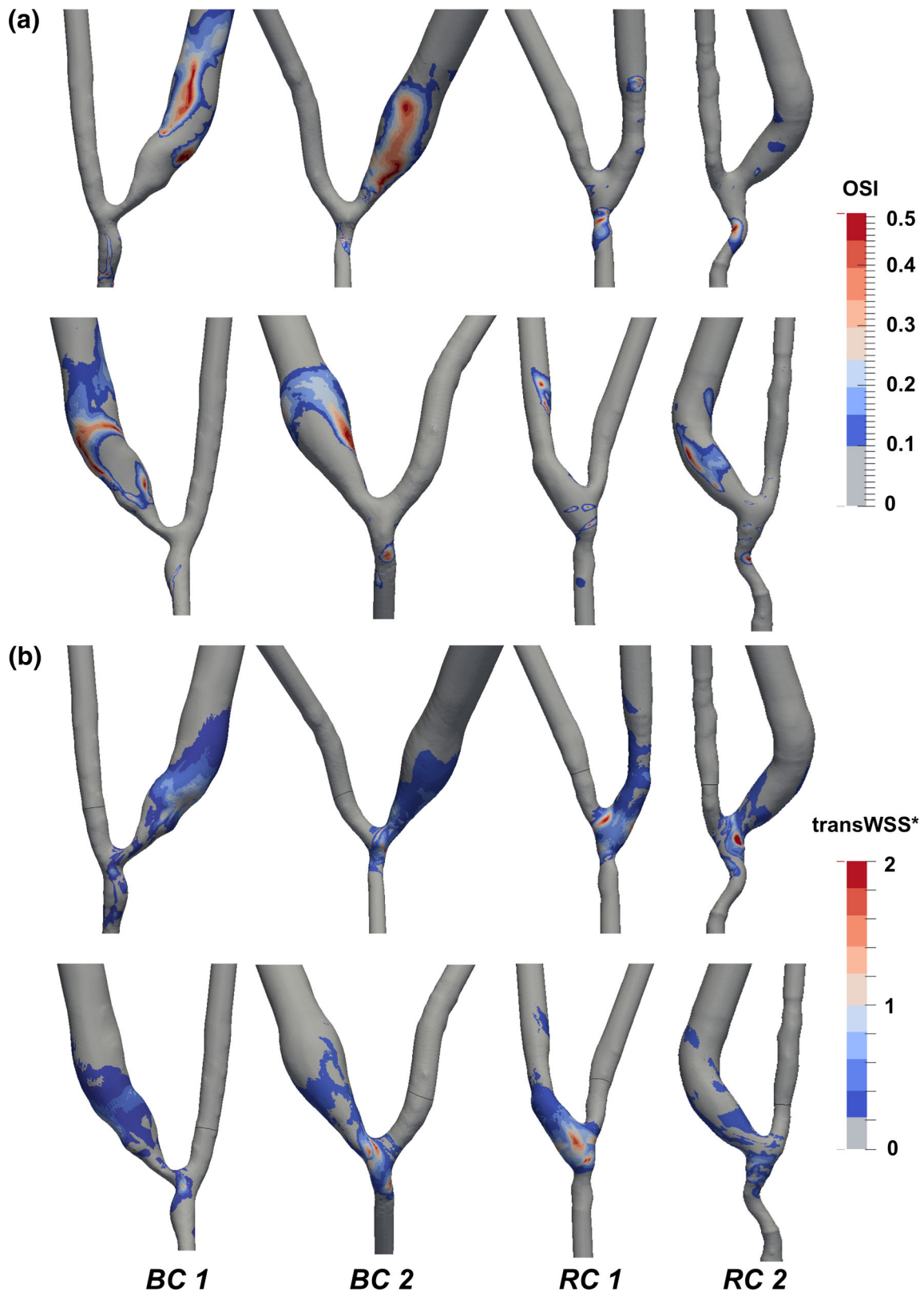
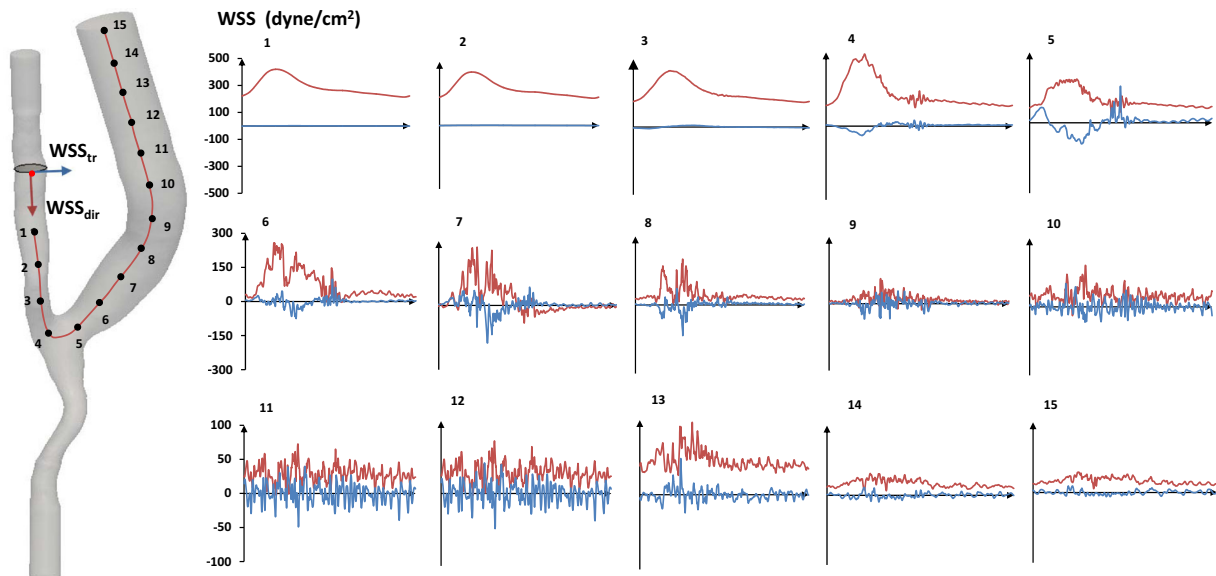


FIGURE 6. (a) Plot of OSI and (b) transWSS\* surface maps on the AVF models. Note: values of OSI between 0 and 0.1 and transWSS\* between 0 and 0.2 were represented in light grey to emphasize the pattern of reciprocating and multidirectional disturbed flow on the AVF surfaces. transWSS\* was normalized by the time-averaged WSS (TAWSS) calculated approximately two diameters far from the anastomosis on the PA (note the clip plane on the transWSS images)



**FIGURE 7.**  $WSS_{dir}$  and  $WSS_{tr}$  traces throughout the cardiac cycle in 15 feature points on the wall alongside the PA and the JAV limbs of the RC 2 AVF model.  $WSS$  Wall shear stress,  $WSS_{dir}$  component of WSS in the mean WSS direction,  $WSS_{tr}$  component of WSS in the direction normal to the temporal mean vector

We have previously suggested that low and oscillating shear stress acting on the EC may induce cell dysfunction responsible for vessel wall changes that may initiate and sustain NH.<sup>46</sup> Actually, while unidirectional and pulsatile blood flow acting on EC maintains physiological vascular structure and function,<sup>11</sup> it is known that the transition of flow to turbulence may trigger cellular events, previously demonstrated *in vitro* on EC. In details, exposure of EC to turbulent shear stress significantly influences EC turnover<sup>12</sup> and impairs production of nitric oxide.<sup>42</sup> On the basis of our actual findings, we may speculate on the mechanisms of AVF remodeling. The findings that oscillatory flow has pro-inflammatory effects when acting perpendicularly to the cell axis defined by their shape and cytoskeleton *in vitro*,<sup>45,53</sup> as well as *in vivo* in the rabbit aorta,<sup>38,44</sup> indicate the multidirectionality of WSS vector as the upstream event that triggers NH. Our study consistently revealed transition from laminar to turbulent-like flow and the existence of high frequency, multidirectional disturbed flow in the JAV. We may thus speculate that is the transitional flow the key hemodynamic factor leading to AVF stenosis and failure of the VA. This is in line with an *in vivo* study by Fillinger *et al.*<sup>18</sup> that found less NH in banded respect to unbanded AVG in canine model. They found that Reynolds number has the best correlation with the development of NH, concluding that “flow disturbance or turbulence” is a major factor of this form of hyperplasia. Moreover, while it is well known that laminar and unidirectional flow induces increase in Krüppel-like factor 2 (KLF2) mRNA

expression,<sup>10</sup> disturbed shear stress obtained by increasing the diameter of a mouse aorto-caval AVF reduced expression of KLF2.<sup>54</sup>

Few data exist in literature on the effect of multidirectional WSS. Mohamied *et al.*<sup>38</sup> found that atherosclerotic lesion prevalence correlated strongly and significantly with transWSS, while correlations with the other shear metrics were not significant or significantly lower. Recently, Jia *et al.* found that NH predisposed to occur on the inner wall of the JAV in a canine model of AVF where multidirectional disturbed flow developed.<sup>25</sup> Further *in vitro* and *in vivo* studies are required to better characterize the effect of multidirectional flow on EC functions that may be relevant for NH, such as adhesion of circulating cells to EC and regulation of SMC proliferation.

The high frequency shear oscillations on the JAV wall, having a low time-averaged WSS, may also trigger or enhance venous NH. A similar conclusion was achieved by Himburg and Friedman<sup>23</sup> showing that regions of porcine iliac arteries with increased endothelial permeability are exposed to higher frequency oscillations in shear stress. Another important aspect of the flow conditions we have characterized on EC surface is the presence of very high values of WSS, especially on the PA. Thus, while it is generally indicated that physiological arterial WSS is within a range of 10–70 dynes/cm<sup>2</sup>,<sup>32</sup> we calculated values of WSS up to 200 dynes/cm<sup>2</sup> in average, in line with findings of other groups.<sup>35,50</sup> Of interest, these very high shear stress areas are not related to vessel changes, likely because the flow is unidirectional, allowing EC to adapt to this mechanical load.

Among the limitations of our study, we have to mention that CFD simulations did not account for the effect of the vessel wall compliance on WSS distribution. This issue could be addressed in future studies by conducting fluid–solid interaction (FSI) analysis, although McGah *et al.*,<sup>34</sup> determined that rigid-walls hemodynamic simulations can predict blood hemodynamics within the same order of accuracy of the FSI equivalent simulations. However, the higher computational cost of this type of analysis renders its clinical use still challenging.<sup>13</sup> The lack of longitudinal patient data has also to be recognized as a limit. A matter of concern may be the high discretization errors we have found in the JAV (Table 2). However, the uncertainties were low in the PA and this might be an indirect confirmation of the development of turbulent-like flow in the JAV. The fact is that modelling of turbulence is challenging and can involve important errors.<sup>29</sup> We advocate the need of future DNS or numerical studies, including turbulence models, to elucidate if our high-resolution CFD simulations can well detect the flow instabilities in AVF for HD.

In conclusion, our pilot, non-invasive study successfully characterized patient-specific flow phenotype and near-wall disturbed flow within the AVF, using image-based CFD analysis. We demonstrated that in the anastomotic region and in the JAV transition from laminar to turbulent-like flows develop, exposing ECs to high-frequency multidirectional disturbed flow. Further studies are needed to shed more light on the relation between these non-physiological flow patterns and development of vascular changes such as NH. From the clinical perspective, we may hypothesize that identification of flow instability in AVF using CFD may allow to identify VA at risk of developing NH and deserving monitoring or intervention to prevent AVF failure.

#### ELECTRONIC SUPPLEMENTARY MATERIAL

The online version of this article (doi: [10.1007/s10439-015-1525-y](https://doi.org/10.1007/s10439-015-1525-y)) contains supplementary material, which is available to authorized users.

#### ACKNOWLEDGMENTS

We thank Prof. Gabriele Dubini from Politecnico di Milano for helpful discussion. We acknowledge the ARCH Consortium colleagues for gaining the CE-MRA data during the clinical study (ARCH Project No. FP7-ICT-224390). Part of this study was presented at the 41st Annual ESAO Congress in Rome, Italy.

#### REFERENCES

- Al-Jaishi, A. A., M. J. Oliver, S. M. Thomas, C. E. Lok, J. C. Zhang, A. X. Garg, S. D. Kosa, R. R. Quinn, and L. M. Moist. Patency rates of the arteriovenous fistula for hemodialysis: a systematic review and meta-analysis. *Am J Kidney Dis* 63:464–478, 2014.
- Antiga, L., M. Piccinelli, L. Botti, B. Ene-Iordache, A. Remuzzi, and D. A. Steinman. An image-based modeling framework for patient-specific computational hemodynamics. *Med Biol Eng Comput* 46:1097–1112, 2008.
- Badero, O. J., M. O. Salifu, H. Wasse, and J. Work. Frequency of swing-segment stenosis in referred dialysis patients with angiographically documented lesions. *Am J Kidney Dis* 51:93–98, 2008.
- Bennett, S., M. S. Hammes, T. Blicharski, S. Watson, and B. Funaki. Characterization of the cephalic arch and location of stenosis. *J Vasc Access* 16:13–18, 2015.
- Bode, A., A. Caroli, W. Huberts, N. Planken, L. Antiga, M. Bosboom, A. Remuzzi, and J. Tordoir. Clinical study protocol for the ARCH project—computational modeling for improvement of outcome after vascular access creation. *J Vasc Access* 12:369–376, 2011.
- Bode, A. S., R. N. Planken, M. A. Merckx, F. M. van der Sande, L. Geerts, J. H. Tordoir, and T. Leiner. Feasibility of non-contrast-enhanced magnetic resonance angiography for imaging upper extremity vasculature prior to vascular access creation. *Eur J Vasc Endovasc Surg* 43:88–94, 2012.
- Browne, L. D., M. T. Walsh, and P. Griffin. Experimental and numerical analysis of the bulk flow parameters within an arteriovenous fistula. *Cardiovasc Eng Technol* 6:450–462, 2015.
- Caroli, A., S. Manini, L. Antiga, K. Passera, B. Ene-Iordache, S. Rota, G. Remuzzi, A. Bode, J. Leermakers, F. N. van de Vosse, R. Vanholder, M. Malovrh, J. Tordoir, and A. Remuzzi. Validation of a patient-specific hemodynamic computational model for surgical planning of vascular access in hemodialysis patients. *Kidney Int* 84:1237–1245, 2013.
- Celik, I. B., U. Ghia, P. J. Roache, C. J. Freitas, H. Coleman, and P. E. Raad. Procedure for estimation and reporting of uncertainty due to discretization in CFD applications. *J Fluids Eng* 130:1–4, 2008.
- Chiu, J. J., and S. Chien. Effects of disturbed flow on vascular endothelium: pathophysiological basis and clinical perspectives. *Physiol Rev* 91:327–387, 2011.
- Davies, P. F. Hemodynamic shear stress and the endothelium in cardiovascular pathophysiology. *Nat Clin Pract Cardiovasc Med* 6:16–26, 2009.
- Davies, P. F., A. Remuzzi, E. J. Gordon, C. F. Dewey, Jr, and M. A. Gimbrone, Jr. Turbulent fluid shear stress induces vascular endothelial cell turnover in vitro. *Proc Natl Acad Sci USA* 83:2114–2117, 1986.
- Decorato, I., Z. Kharboutly, T. Vassallo, J. Penrose, C. Legallais, and A. V. Salsac. Numerical simulation of the fluid structure interactions in a compliant patient-specific arteriovenous fistula. *Int J Numer Method Biomed Eng* 30:143–159, 2014.
- Ene-Iordache, B., L. Mosconi, L. Antiga, S. Bruno, A. Anghileri, G. Remuzzi, and A. Remuzzi. Radial artery remodeling in response to shear stress increase within arteriovenous fistula for hemodialysis access. *Endothelium* 10:95–102, 2003.
- Ene-Iordache, B., and A. Remuzzi. Disturbed flow in radial-cephalic arteriovenous fistulae for haemodialysis: low



- and oscillating shear stress locates the sites of stenosis. *Nephrol Dial Transplant* 27:358–368, 2012.
- <sup>16</sup>Ene-Iordache, B., C. Semperboni, G. Dubini, and A. Remuzzi. Disturbed flow in a patient-specific arteriovenous fistula for hemodialysis: multidirectional and reciprocating near-wall flow patterns. *J Biomech* 48:2195–2200, 2015.
  - <sup>17</sup>Fan, L., and T. Karino. Effect of a disturbed flow on proliferation of the cells of a hybrid vascular graft. *Biorheology* 47:31–38, 2010.
  - <sup>18</sup>Fillinger, M. F., E. R. Reinitz, R. A. Schwartz, D. E. Resetarits, A. M. Paskanik, and C. E. Bredenberg. Beneficial effects of banding on venous intimal-medial hyperplasia in arteriovenous loop grafts. *Am J Surg* 158:87–94, 1989.
  - <sup>19</sup>Gallo, D., D. A. Steinman, P. B. Bijari, and U. Morbiducci. Helical flow in carotid bifurcation as surrogate marker of exposure to disturbed shear. *J Biomech* 45:2398–2404, 2012.
  - <sup>20</sup>Gimbrone, Jr., M. A., and G. Garcia-Cardena. Vascular endothelium, hemodynamics, and the pathobiology of atherosclerosis. *Cardiovasc Pathol* 22:9–15, 2013.
  - <sup>21</sup>He, X., and D. N. Ku. Pulsatile flow in the human left coronary artery bifurcation: average conditions. *J Biomech Eng* 118:74–82, 1996.
  - <sup>22</sup>He, Y., C. M. Terry, C. Nguyen, S. A. Berceci, Y. T. Shiu, and A. K. Cheung. Serial analysis of lumen geometry and hemodynamics in human arteriovenous fistula for hemodialysis using magnetic resonance imaging and computational fluid dynamics. *J Biomech* 46:165–169, 2013.
  - <sup>23</sup>Himburg, H. A., and M. H. Friedman. Correspondence of low mean shear and high harmonic content in the porcine iliac arteries. *J Biomech Eng* 128:852–856, 2006.
  - <sup>24</sup>Jha, V., G. Garcia-Garcia, K. Iseki, Z. Li, S. Naicker, B. Plattner, R. Saran, A. Y. Wang, and C. W. Yang. Chronic kidney disease: global dimension and perspectives. *Lancet* 382:260–272, 2013.
  - <sup>25</sup>Jia, L., L. Wang, F. Wei, H. Yu, H. Dong, B. Wang, Z. Lu, G. Sun, H. Chen, J. Meng, B. Li, R. Zhang, X. Bi, Z. Wang, H. Pang, and A. Jiang. Effects of wall shear stress in venous neointimal hyperplasia of arteriovenous fistulae. *Nephrology (Carlton)* 20:335–342, 2015.
  - <sup>26</sup>Khan, M. O., K. Valen-Sendstad, and D. A. Steinman. Narrowing the expertise gap for predicting intracranial aneurysm hemodynamics: impact of solver numerics versus mesh and time-step resolution. *AJNR Am J Neuroradiol* 36:1310–1316, 2015.
  - <sup>27</sup>Lee, T., V. Chauhan, M. Krishnamoorthy, Y. Wang, L. Arend, M. J. Mistry, M. El-Khatib, R. Banerjee, R. Munda, and P. Roy-Chaudhury. Severe venous neointimal hyperplasia prior to dialysis access surgery. *Nephrol Dial Transplant* 26:2264–2270, 2011.
  - <sup>28</sup>Lee, S. W., D. S. Smith, F. Loth, P. F. Fischer, and H. S. Bassiouny. Importance of flow division on transition to turbulence within an arteriovenous graft. *J Biomech* 40:981–992, 2007.
  - <sup>29</sup>Leschziner, M. Statistical turbulence modelling for fluid dynamics—demystified: an introductory text for graduate engineering students. London: Imperial College Press, 2015.
  - <sup>30</sup>Lorensen, W. E., and H. E. Cline. Marching cubes: a high resolution 3D surface construction algorithm. *Computer Graphics* 21:163–169, 1987.
  - <sup>31</sup>Loth, F., P. F. Fischer, N. Arslan, C. D. Bertram, S. E. Lee, T. J. Royston, W. E. Shaalan, and H. S. Bassiouny. Transitional flow at the venous anastomosis of an arteriovenous graft: potential activation of the ERK1/2 mechanotransduction pathway. *J Biomech Eng* 125:49–61, 2003.
  - <sup>32</sup>Malek, A. M., S. L. Alper, and S. Izumo. Hemodynamic shear stress and its role in atherosclerosis. *JAMA* 282:2035–2042, 1999.
  - <sup>33</sup>Marie, Y., A. Guy, K. Tullett, H. Krishnan, R. G. Jones, and N. G. Inston. Patterns of blood flow as a predictor of maturation of arteriovenous fistula for haemodialysis. *J Vasc Access* 15:169–174, 2014.
  - <sup>34</sup>McGah, P. M., D. F. Leotta, K. W. Beach, and A. Aliseda. Effects of wall distensibility in hemodynamic simulations of an arteriovenous fistula. *Biomech Model Mechanobiol* 13:679–695, 2014.
  - <sup>35</sup>McGah, P. M., D. F. Leotta, K. W. Beach, R. Eugene Zierler, and A. Aliseda. Incomplete restoration of homeostatic shear stress within arteriovenous fistulae. *J Biomech Eng* 135:011005, 2013.
  - <sup>36</sup>Mitra, A. K., D. M. Gangahar, and D. K. Agrawal. Cellular, molecular and immunological mechanisms in the pathophysiology of vein graft intimal hyperplasia. *Immunol Cell Biol* 84:115–124, 2006.
  - <sup>37</sup>Moffatt, H. K., and A. Tsinober. Helicity in laminar and turbulent flow. *Ann Rev Fluid Mech* 24:281–312, 1992.
  - <sup>38</sup>Mohamied, Y., E. M. Rowland, E. L. Bailey, S. J. Sherwin, M. A. Schwartz, and P. D. Weinberg. Change of direction in the biomechanics of atherosclerosis. *Ann Biomed Eng* 43:16–25, 2015.
  - <sup>39</sup>Morbiducci, U., R. Ponzini, D. Gallo, C. Bignardi, and G. Rizzo. Inflow boundary conditions for image-based computational hemodynamics: impact of idealized versus measured velocity profiles in the human aorta. *J Biomech* 46:102–109, 2013.
  - <sup>40</sup>Morbiducci, U., R. Ponzini, M. Grigioni, and A. Redaelli. Helical flow as fluid dynamic signature for atherogenesis risk in aortocoronary bypass. A numeric study. *J Biomech* 40:519–534, 2007.
  - <sup>41</sup>NKF, KDOQI. Clinical practice guidelines for vascular access. *Am J Kidney Dis* 48:S248–S273, 2006.
  - <sup>42</sup>Noris, M., M. Morigi, R. Donadelli, S. Aiello, M. Foppolo, M. Todeschini, S. Orisio, G. Remuzzi, and A. Remuzzi. Nitric oxide synthesis by cultured endothelial cells is modulated by flow conditions. *Circ Res* 76:536–543, 1995.
  - <sup>43</sup>OpenFoam. The OpenFOAM Foundation. <http://www.openfoam.org>, 2014.
  - <sup>44</sup>Peiffer, V., S. J. Sherwin, and P. D. Weinberg. Computation in the rabbit aorta of a new metric—the transverse wall shear stress—to quantify the multidirectional character of disturbed blood flow. *J Biomech* 46:2651–2658, 2013.
  - <sup>45</sup>Potter, C. M., M. H. Lundberg, L. S. Harrington, C. M. Warboys, T. D. Warner, R. E. Berson, A. V. Moshkov, J. Gorelik, P. D. Weinberg, and J. A. Mitchell. Role of shear stress in endothelial cell morphology and expression of cyclooxygenase isoforms. *Arterioscler Thromb Vasc Biol* 31:384–391, 2011.
  - <sup>46</sup>Remuzzi, A., and B. Ene-Iordache. Novel paradigms for dialysis vascular access: upstream hemodynamics and vascular remodeling in dialysis access stenosis. *Clin J Am Soc Nephrol* 8:2186–2193, 2013.
  - <sup>47</sup>Remuzzi, A., B. Ene-Iordache, L. Mosconi, S. Bruno, A. Anghileri, L. Antiga, and G. Remuzzi. Radial artery wall shear stress evaluation in patients with arteriovenous fistula for hemodialysis access. *Biorheology* 40:423–430, 2003.
  - <sup>48</sup>Roy-Chaudhury, P., Y. Wang, M. Krishnamoorthy, J. Zhang, R. Banerjee, R. Munda, S. Heffelfinger, and L.



- Arend. Cellular phenotypes in human stenotic lesions from haemodialysis vascular access. *Nephrol Dial Transplant* 24:2786–2791, 2009.
- <sup>49</sup>Sethian, J. A. Level set methods and marching cubes methods: evolving interfaces in computational geometry, fluid mechanics, computer vision and materials science, Vol. 3. Cambridge: Cambridge University Press, 1999.
- <sup>50</sup>Sigovan, M., V. Rayz, W. Gasper, H. F. Alley, C. D. Owens, and D. Saloner. Vascular remodeling in autogenous arterio-venous fistulas by MRI and CFD. *Ann Biomed Eng* 41:657–668, 2013.
- <sup>51</sup>Valen-Sendstad, K., M. Piccinelli, and D. A. Steinman. High-resolution computational fluid dynamics detects flow instabilities in the carotid siphon: implications for aneurysm initiation and rupture? *J Biomech* 47:3210–3216, 2014.
- <sup>52</sup>Van Canneyt, K., U. Morbiducci, S. Eloot, G. De Santis, P. Segers, and P. Verdonck. A computational exploration of helical arterio-venous graft designs. *J Biomech* 46:345–353, 2013.
- <sup>53</sup>Wang, C., B. M. Baker, C. S. Chen, and M. A. Schwartz. Endothelial cell sensing of flow direction. *Arterioscler Thromb Vasc Biol* 33:2130–2136, 2013.
- <sup>54</sup>Yamamoto, K., C. D. Protack, G. Kuwahara, M. Tsuneki, T. Hashimoto, M. R. Hall, R. Assi, K. E. Brownson, T. R. Foster, H. Bai, M. Wang, J. A. Madri, and A. Dardik. Disturbed shear stress reduces Klf2 expression in arterial-venous fistulae in vivo. *Physiol Rep* 3:e12348, 2015.
- <sup>55</sup>Yang, N., S. Deutsch, E. G. Paterson, and K. B. Manning. Numerical study of blood flow at the end-to-side anastomosis of a left ventricular assist device for adult patients. *J Biomech Eng* 131:111005, 2009.